ChemComm

COMMUNICATION

View Article Online
View Journal | View Issue

Cite this: *Chem. Commun.*, 2025, **61**, 2989

Received 4th December 2024,
Accepted 17th January 2025

DOI: 10.1039/d4cc06411a

rsc.li/chemcomm

Deep eutectic solvent-assisted recycling of spent lithium-ion batteries into electrocatalysts for polyethylene terephthalate upcycling†

Xinhui Zhao, * Cheng Kuang, Rujin Zhou, Nina Yang, Chaopeng An, Jing Xu and Mingyan Wang

We propose an effective method for selectively extracting the valuable metals from the spent $LiNi_xCo_yMn_{1-x-y}O_2$ cathode material using an oxalic acid-based deep eutectic solvent. Through regulation of the coordination environment, NiO, Co_3O_4, and Mn_3O_4 are stepwise separated and further applied in the electrochemical conversion of raw PET bottles to high-purity formic acid.

Polyethylene terephthalate (PET), a widely used polyester plastic, decomposes very slowly in nature. As a result, improper disposal of PET plastic waste leads to serious environmental pollution and a considerable loss of carbon resources.[1] Since traditional mechanical recycling typically results in the degradation of plastic properties, there is an urgent need to develop more environmentally and economically sustainable methods for recycling PET waste.[2] The electrochemical strategy has recently emerged as a promising route for PET upcycling, with the characteristics of being renewable electricity-driven, ambient reaction conditions, and value-added products.[3] In this process, PET is first converted into terephthalate and ethylene glycol (EG) monomers through alkaline hydrolysis. Subsequently, high-purity terephthalic acid (TPA) could be easily isolated from the solution by adjusting the pH value, while the remaining EG can be electrochemically oxidized to form high-value formate/formic acid (HCOOH). This innovative system highlights the significant potential of electrocatalysis in PET plastics recycling. Therefore, researchers have sought to develop selective and efficient transition metal-based electrocatalysts to provide a more cost-effective pathway for PET upcycling.[4–6]

As the demand for sustainable and cost-effective materials for energy and environmental applications has grown, extensive research has focused on utilizing low-cost and eco-friendly solutions. In this respect, waste-derived or biosourced materials including lignin, cyclodextrins, and humic-like substances are being explored for use in catalysis, energy storage systems, and sewage treatment.[7–12] Recently, there has been significant progress in the synthesis of transition metal nanomaterials derived from spent lithium-ion batteries (LIBs).[13–16] For example, Chen *et al.*[17] employed a simple one-pot boronization process to recover spent LIBs and convert them into mixed metal boride (NiCoMnBs) catalyst materials with metal ion recoveries of 99.91%, 99.92%, and 99.84% for Ni, Co, and Mn, respectively. In another approach, Yang *et al.*[18] utilized a sulfuric acid etchant to recycle both the Al current collector and anode materials and prepared Al-doped $LiNi_{0.9}Co_{0.05}Mn_{0.05}O_2$ with improved electrochemical performance. Although significant progress has been made, most recycling processes still rely on mineral acids. Therefore, there is a growing need for simple, cost-effective, and environmentally friendly methods to selectively separate transition metals from spent LIB cathodes.

Deep eutectic solvents (DESs) are an emerging versatile solvent, formed by the combination of a quaternary ammonium salt and a hydrogen bond donor. DESs share many characteristics with ionic liquids, but their low cost and simple preparation make them particularly attractive for a range of applications, including metal recovery and plastic depolymerization.[19–23] In our previous reports, we developed a DES composed of choline chloride and oxalic acid dehydrate (ChCl:OxA) for the extraction of cobalt from spent $LiCoO_2$ cathodes, which was subsequently recovered as cobalt oxalate.[24,25] Building on these findings, we now extend this approach to extract multiple metals from the ternary cathode material $LiNi_xCo_yMn_{1-x-y}O_2$ (NCM). However, due to the similar physicochemical properties of the transition metals, selectively separating Ni, Co, and Mn within this DES presents significant challenges.

In this study, we explore the selective extraction of multiple transition metals from spent NCM using ChCl:OxA DES. By regulating the coordination environment, Ni, Co, and Mn are successfully stepwise separated, owing to their distinct solubilities in the DES system. The as-collected precipitates are then

Jiangsu Key Laboratory of Function Control Technology for Advanced Materials, School of Environmental and Chemical Engineering Jiangsu Ocean University Lianyungang, Jiangsu 222005, China. E-mail: xhzhao@jou.edu.cn

† Electronic supplementary information (ESI) available: Experiment section, SEM images, XRD patterns, and XPS spectra. See DOI: https://doi.org/10.1039/d4cc06411a

processed to yield NiO, Co_3O_4, and Mn_3O_4. Moreover, we demonstrate that these metal oxides can efficiently catalyze the electro-reforming waste PET into terephthalic acid and formic acid with high efficiency.

The DES was synthesized by heating a mixture of choline chloride and oxalic acid dihydrate (ChCl:OxA) at 60 °C until a clear and transparent liquid formed. The hydrogen bond interactions between ChCl and OxA in the DES were investigated using Fourier transform infrared spectroscopy (FT-IR). As shown in Fig. S1 (ESI†), the mixture retains the characteristic peaks of each component, while the C═O vibration of oxalic acid exhibits a blue shift, suggesting the formation of the DES. We then proposed a method for the stepwise separation of nickel, cobalt, and manganese from spent $LiNi_xCo_yMn_{1-x-y}O_2$ (NCM) materials based on the different solubility of their oxalates in the prepared DES. The whole recycling route is illustrated in Fig. 1.

First, the collected NCM powders are added to the prepared DES. After leaching at 120 °C for 10 h, the initially colorless transparent DES becomes cloudy, forming a blue-green precipitate (Fig. S2, ESI†). According to previous reports, nickel dissolved in the oxalic acid-based DES tends to precipitate as NiC_2O_4, while cobalt and manganese remain as complexes within the DES.[24] Therefore, nickel is separated as $NiC_2O_4{\cdot}2H_2O$ (product 2) by diluting the DES, followed by vacuum filtration. Next, we add water to dilute the filtrate and heat at 70 °C for 3 h to precipitate cobalt as $CoC_2O_4{\cdot}2H_2O$ (product 4). In the third step, manganese oxide mixtures (product 6) are separated from the final solution by adjusting the pH to 12 using KOH. Finally, the corresponding metal precursors are calcined at the desired temperature to form NiO, Co_3O_4, and Mn_3O_4 for better characteristics and application.

To improve metal separation, we selected DMSO to reduce the viscosity of the system prior to the first step. After the nickel separation, the diluted filtrate (product 3) appears a blue color, as shown on the left in Fig. 2a. This observation indicates that the introduction of DMSO does not interfere with the complexes of cobalt and manganese. The blue color is attributed to the formation of tetrahedron $[CoCl_4]^{2-}$, which is verified by three characteristic absorption bands at 634, 667, and 693 nm in the UV/vis spectrum (Fig. 2b, black line).[25] To separate cobalt, we introduced water to change the coordination

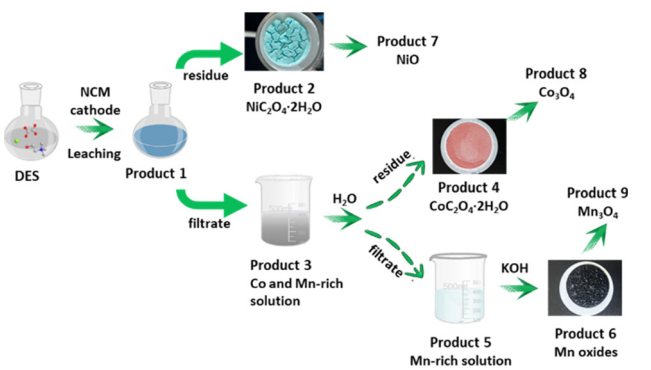

Fig. 1 Flowchart for selective separation and recovery of spent LIBs.

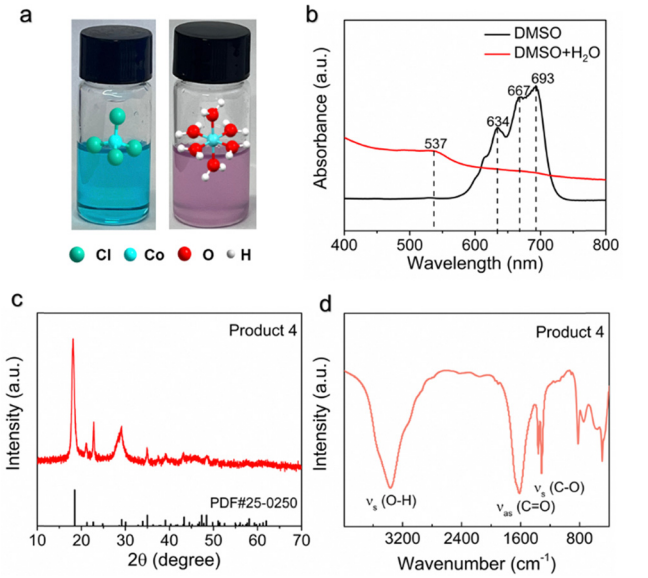

Fig. 2 (a) Photograph of the filtrate (left) diluted by DMSO and filtrate (right) diluted by DMSO and H_2O. (b) UV/vis spectra of the filtrate. (c) XRD pattern and (d) FT-IR spectrum of product 4.

structure of cobalt, resulting in the formation of the new octahedral $[Co(H_2O)_6]^{2+}$ complex. As a result, the color of the solution immediately changed from blue to pink (shown on the right in Fig. 2a), and the corresponding characteristic peak appeared at 537 nm in the UV/vis spectrum (Fig. 2b, red line). According to previous reports, Co^{2+} tends to combine with $C_2O_4^{2-}$ to form cobalt oxalate precipitation in oxalic acid-based solutions. To expedite this process, we heated the solution at 70 °C for 5 h and subsequently isolated the cobalt as a pink precipitate (product 4). Product 4 was confirmed to be $CoC_2O_4{\cdot}2H_2O$ according to the XRD results (Fig. 2c). The FT-IR spectrum of product 4 (Fig. 2d) displays characteristic peaks at 3372 cm^{-1} (O–H stretching), 1617 cm^{-1} (C═O antisymmetric stretching), 1359 and 1317 cm^{-1} (C–O symmetric stretching), which align with the expected functional groups of $CoC_2O_4{\cdot}2H_2O$.[26] The detailed separation mechanism of nickel and manganese is discussed in the ESI.†

To obtain pure Co_3O_4, we then calcined product 4 at 500 °C for 2 h, as confirmed by the XRD pattern in Fig. S6 (ESI†).[27] The chemical composition and oxidation state of the obtained Co_3O_4 (product 8) were further analyzed by XPS. The Co 2p spectrum (Fig. S7a, ESI†) shows a distinct splitting of the Co 2p band into Co $2p_{3/2}$ and Co $2p_{1/2}$, with peaks centered at 779.2 eV and 794.6 eV, respectively. The existence of both Co^{2+} and Co^{3+} species is confirmed by two asymmetric spin–orbit doublet peaks, accompanied by faint satellite oscillation peaks. This result is further supported by the O 1s XPS spectrum (Fig. S7b, ESI†), where the characteristic peak at 529.4 eV confirms the formation of Co_3O_4.[28] High-resolution SEM images show that the prepared Co_3O_4 material has an irregular rod-like structure with small pores on the surface (Fig. 3a and b). EDS elemental mapping indicates a uniform distribution of Co and O elements in Co_3O_4 (Fig. 3c–e).

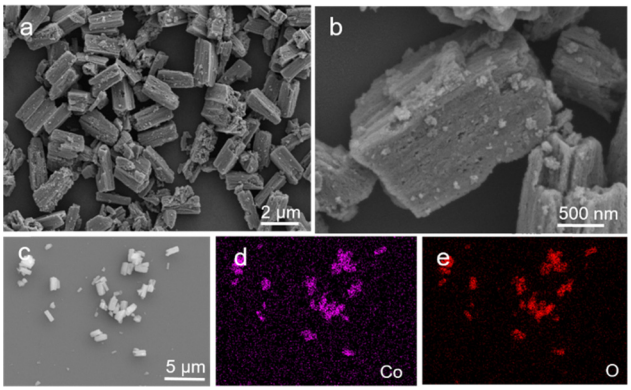

Fig. 3 (a) and (b) SEM images and (c)–(e) EDS elemental mapping of product 8.

The electrocatalytic activity of the three metal oxide materials was evaluated in a 1.0 M KOH solution containing 0.1 M PET hydrolysate using a standard three-electrode system. The PET hydrolysate was prepared by KOH-catalyzed hydrolysis of a real-world PET bottle at 180 °C for 4 h (Fig. S11, ESI†). The working electrode was fabricated by uniformly depositing catalyst inks onto nickel foam (NF). Linear sweep voltammetry (LSV) was performed at a scan rate of 5 mV s^{-1} to assess the electrocatalytic activity of the three samples for PET oxidation. Fig. 4a presents the LSV curves of the three materials in a 1 M KOH solution containing 0.1 M PET hydrolysate. It is clear that Co_3O_4 exhibits a significantly lower potential for PET hydrolysate oxidation. Therefore, the Co_3O_4 material was selected as the representative catalyst to evaluate the differences between the oxygen evolution reaction (OER) and the ethylene glycol oxidation reaction (EGOR). As shown in Fig. 4b, the Co_3O_4 catalyst achieves a current density of 50 mA cm^{-2} at 1.33 V *vs.* RHE in PET hydrolysate, representing a significant reduction of 380 mV compared to the OER. These results indicate that EGOR is thermodynamically more favorable than the OER. Control experiments conducted under various conditions further confirm that the current density remains almost identical with or without the presence of TPA, suggesting that the enhanced catalytic current is attributed to the oxidation of EG derived from PET hydrolysis (Fig. S12–S14, ESI†).

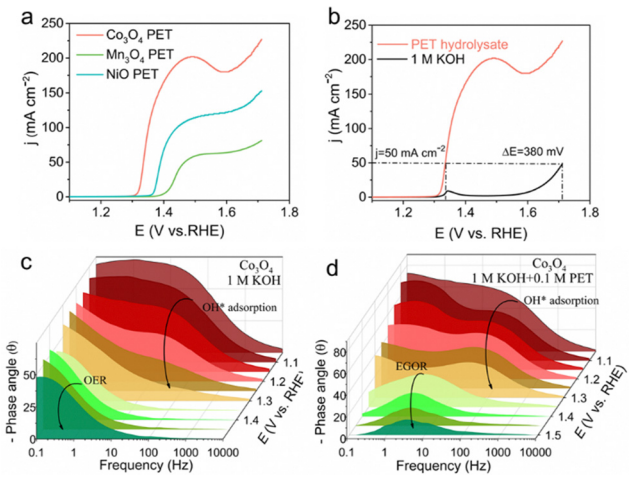

Fig. 4 (a) LSV curves of NiO, Co_3O_4, and Mn_3O_4 catalysts in 1.0 M KOH with 0.1 M PET. (b) LSV curves of the Co_3O_4 catalyst in 1.0 M KOH with or without 0.1 M PET. Bode phase plots of the *in situ* EIS on Co_3O_4 in (c) 1.0 M KOH and (d) 1.0 M KOH with 0.1 M PET.

To further investigate the catalytic kinetics of the obtained materials, Tafel plots derived from the LSV curves are presented in Fig. S15 (ESI†). All catalysts show lower Tafel slopes in the PET hydrolysate compared to the KOH solution, consistent with the LSV curves. As expected, the Co_3O_4 catalyst exhibits the smallest Tafel slope of 36 mV dec^{-1} in the PET hydrolysate, while the Tafel slopes for NiO and Mn_3O_4 are 38 mV dec^{-1} and 45 mV dec^{-1}, respectively. Based on the cyclic voltammetry curves at different scanning rates in Fig. S16a–c (ESI†), the Co_3O_4 electrode exhibits a high double-layer capacitance (C_{dl}) of 1.43 mF cm^{-2} (Fig. S16d, ESI†). This suggests that Co_3O_4 has favorable electrochemical catalytic active sites for the EGOR.

To investigate the interfacial behaviors between the electrode and electrolyte, we performed *in situ* electrochemical impedance spectroscopy (EIS) at various potentials. As shown in Fig. 4c and d, the Co_3O_4 catalyst exhibits characteristic peaks around 100 Hz in the potential range of 1.05 to 1.3 V *vs.* RHE, which are assigned to the adsorption of OH^- reactants in the 1 M KOH solution. These peaks are also observed in the PET hydrolysate, indicating similar electrochemical interface behavior between OER and EGOR at low applied potentials. As the applied potential reaches 1.35 V *vs.* RHE, a new peak emerges in the low-frequency region (0.1–10 Hz) in 1 M KOH, indicating the onset of the OER. In contrast, a different peak (1–10 Hz) is observed at 1.3 V *vs.* RHE in PET hydrolysate, which is ascribed to the onset of the EGOR. Similar Bode phase plots are also observed for NiO and Mn_3O_4 (Fig. S17, ESI†). Meanwhile, all catalysts exhibit lower electron transfer resistance (R_{ct}) in PET hydrolysate, suggesting enhanced electron transfer kinetics compared to the OER (Fig. S18, ESI†). Additionally, the R_{ct} values decrease as the applied potential increases from 1.05 to 1.55 V *vs.* RHE. Furthermore, we performed open-circuit potential (OCP) to monitor the adsorption behavior of the prepared materials in the inner Helmholtz layer (Fig. S19, ESI†).[29,30] Upon adding 0.3 M EG to the solution, a noticeable decrease in OCP was observed for all catalysts. As expected, the Co_3O_4 catalyst showed the largest decrease of 83 mV, greater than the decreases observed for NiO (29.7 mV) and Mn_3O_4 (41 mV). This suggests that a dominant number of EG molecules are adsorbed within the inner Helmholtz layer on the Co_3O_4 surface. The results clearly demonstrate the strong adsorption of EG and OH^- on the Co_3O_4 catalyst, which contributes to its superior performance in the EGOR.

Building on the foundations established, we aim to upcycle real-world PET plastic and identify the resulting products. Controlled potential electrolysis of the obtained catalyst was performed at various potentials in the PET hydrolysate to determine the products of EGOR. At a potential of 1.51 V *vs.* RHE, after 4 h of electrolysis, the electrolyte was pipetted and analyzed using nuclear magnetic resonance (NMR) spectroscopy

(Fig. S20 and S21, ESI†). The results show that formic acid (FA) is the predominant oxidation product for all catalysts, with no other detectable products present in the electrolyte. We then calculated the faradaic efficiency (FE) of FA using the internal standard method. Each catalyst was repeatedly tested three times to guarantee the reproducibility of the measurement results. The Co_3O_4 catalyst exhibits the highest FE of 90.6% with a concentration of 83 mM of produced FA, outperforming both the NiO (FE: 84.5%) and Mn_3O_4 (FE: 79.8%) catalysts. Fig. S22–S24 (ESI†) show the obvious decline in current density for all catalysts, which is attributed to the consumption of EG during the electrolysis. The exceptional stability of the catalysts is further confirmed by comparing the LSV curves obtained before and after electrolysis.

Due to the different coordination structures of transition metal complexes, nickel, cobalt, and manganese are successfully extracted from spent LIBs using a tandem leaching and separation method. The NiO, Co_3O_4, and Mn_3O_4 materials are then obtained by calcining the recovered metal precipitates. The optimal Co_3O_4 catalyst exhibits a high FE of 90.6% at 1.51 V *vs.* RHE, yielding potassium formate with a concentration of 83 mM. Further in-depth investigations reveal that Co_3O_4 promotes faster charger transfer, increases the electrochemically active area, and enhances absorption of EG molecules and OH^-, all of which synergistically improves its EGOR performance. This study provides a waste-treating-waste strategy for electro-reforming PET plastic into valuable formic acid using spent LIB-derived catalysts.

The authors acknowledge the financial support of the Natural Science Foundation of the Jiangsu Higher Education Institutions of China (No. 22KJB150022).

Data availability

The data supporting this article have been included as part of the ESI.†

Conflicts of interest

There are no conflicts to declare.

Notes and references

1 V. Tournier, C. Topham, A. Gilles, B. David, C. Folgoas, E. Moya-Leclair, E. Kamionka, M.-L. Desrousseaux, H. Texier and S. Gavalda, *Nature*, 2020, **580**, 216–219.
2 I. Vollmer, M. J. F. Jenks, M. C. P. Roelands, R. J. White, T. van Harmelen, P. de Wild, G. P. van der Laan, F. Meirer, J. T. F. Keurentjes and B. M. Weckhuysen, *Angew. Chem., Int. Ed.*, 2020, **59**, 15402–15423.
3 Q. Hu, Z. Zhang, D. He, J. Wu, J. Ding, Q. Chen, X. Jiao and Y. Xie, *J. Am. Chem. Soc.*, 2024, **146**, 16950–16962.
4 M. Song, Y. Wu, Z. Zhao, M. Zheng, C. Wang and J. Lu, *Adv. Mater.*, 2024, **36**, 2403234.
5 J. Wang, X. Li, M. Wang, T. Zhang, X. Chai, J. Lu, T. Wang, Y. Zhao and D. Ma, *ACS Catal.*, 2022, **12**, 6722–6728.
6 Z. Li, Z. Yang, S. Wang, H. Luo, Z. Xue, Z. Liu and T. Mu, *Chem. Eng. J.*, 2024, **479**, 147611.
7 S. Kumar and X. T. Cao, *Coord. Chem. Rev.*, 2024, **499**, 215524.
8 P. García-Negueroles, S. García-Ballesteros, L. Santos-Juanes, C. Sabater, M. A. Castillo, M. F. López-Pérez, R. Vicente, A. M. Amat and A. Arques, *J. Environ. Chem. Eng.*, 2021, **9**, 106862.
9 M. Alidoost, A. Mangini, F. Caldera, A. Anceschi, J. Amici, D. Versaci, L. Fagiolari, F. Trotta, C. Francia, F. Bella and S. Bodoardo, *Chem. – Eur. J.*, 2022, **28**, e202104201.
10 P. Garcia-Negueroles, S. Garcia-Ballesteros, A. M. Amat, E. Laurenti, A. Arques and L. Santos-Juanes, *ACS Omega*, 2019, **4**, 21698–21703.
11 S. Trano, F. Corsini, G. Pascuzzi, E. Giove, L. Fagiolari, J. Amici, C. Francia, S. Turri, S. Bodoardo, G. Griffini and F. Bella, *ChemSusChem*, 2022, **15**, e202200294.
12 Y. Ma, Y. Zhang, W. Yuan, M. Du, S. Kang and B. Qiu, *EES Catal.*, 2023, **1**, 892–920.
13 D. J. Garole, R. Hossain, V. J. Garole, V. Sahajwalla, J. Nerkar and D. P. Dubal, *ChemSusChem*, 2020, **13**, 3079–3100.
14 M. Yang, Y. Sun, S. Lyu, T. Zhang, L. Yang, Z. Li and G. Zhang, *Chem. Commun.*, 2023, **59**, 924–927.
15 J. Liang, K. Li, F. Shi, J. Li, J. N. Gu, Y. Xue, C. Bao, M. Guo, J. Jia, M. Fan and T. Sun, *Angew. Chem., Int. Ed.*, 2024, **63**, e202407870.
16 M. Jiao, Q. Zhang, C. Ye, Z. Liu, X. Zhong, J. Wang, C. Li, L. Dai, G. Zhou and H. M. Cheng, *Proc. Natl. Acad. Sci. U. S. A.*, 2022, **119**, e2202202119.
17 Z. Chen, W. Zou, R. Zheng, W. Wei, W. Wei, B.-J. Ni and H. Chen, *Green Chem.*, 2021, **23**, 6538–6547.
18 T. Wang, L. Wang, C. Yi, W. Sun, M. Wu and Y. Yang, *Chem. Eng. J.*, 2024, **492**, 152298.
19 B. B. Hansen, S. Spittle, B. Chen, D. Poe, Y. Zhang, J. M. Klein, A. Horton, L. Adhikari, T. Zelovich, B. W. Doherty, B. Gurkan, E. J. Maginn, A. Ragauskas, M. Dadmun, T. A. Zawodzinski, G. A. Baker, M. E. Tuckerman, R. F. Savinell and J. R. Sangoro, *Chem. Rev.*, 2021, **121**, 1232–1285.
20 J. Wang, Y. Lyu, R. Zeng, S. Zhang, K. Davey, J. Mao and Z. Guo, *Energy Environ. Sci.*, 2024, **17**, 867–884.
21 M. Guo, R. Deng, M. Gao, C. Xu and Q. Zhang, *Curr. Opin. Green Sustainable Chem.*, 2024, **47**, 100913.
22 A. N. Paparella, S. Perrone, A. Salomone, F. Messa, L. Cicco, V. Capriati, F. M. Perna and P. Vitale, *Catalysts*, 2023, **13**, 1035.
23 Y. Li, M. Sun, Y. Cao, K. Yu, Z. Fan and Y. Cao, *ChemSusChem*, 2024, **17**, e202301953.
24 X. Zhao, C. Kuang, H. Liu, C. An, M. Wang and T. Mu, *ChemSusChem*, 2024, **17**, e202400105.
25 X. Zhao, C. Kuang and C. An, CN Pat., CN117756190A, 2024.
26 J. M. Hartley, C.-M. Ip, G. C. Forrest, K. Singh, S. J. Gurman, K. S. Ryder, A. P. Abbott and G. Frisch, *Inorg. Chem.*, 2014, **53**, 6280–6288.
27 X. Chang, M. Fan, C. F. Gu, W. H. He, Q. Meng, L. J. Wan and Y. G. Guo, *Angew. Chem., Int. Ed.*, 2022, **61**, e202202558.
28 L. Ren, P. Wang, Y. Han, C. Hu and B. Wei, *Chem. Phys. Lett.*, 2009, **476**, 78–83.
29 L. Liu, Z. Jiang, L. Fang, H. Xu, H. Zhang, X. Gu and Y. Wang, *ACS Appl. Mater. Interfaces*, 2017, **9**, 27736–27744.
30 J. Wu, Z. Kong, Y. Li, Y. Lu, P. Zhou, H. Wang, L. Xu, S. Wang and Y. Zou, *ACS Nano*, 2022, **16**, 21518–21526.

